Geophys. J. Int. (1997) **131**, 535–551

Deformation of subducted oceanic lithosphere

Gregory A. Houseman[1,*] and David Gubbins[2]

[1] *Australian Geodynamics Cooperative Research Centre and Department of Mathematics, Monash University, Clayton* VIC 3168, *Australia*
[2] *Department of Earth Sciences, University of Leeds, Leeds* LS2 9JT, *UK*

Accepted 1997 June 16. Received 1997 June 3; in original form 1996 September 23

SUMMARY

The deformation of subducted oceanic lithosphere is revealed by detailed studies of the distribution of seismicity in Benioff zones and by the increasingly well-resolved images of the upper mantle obtained by seismic *P*-wave tomography. By using numerical experiments based on a simplified dynamical model of a subducted lithospheric slab, we test the idea that the observed deformation of the subducted slab results from a balance between internal buoyancy forces and the viscous stresses associated with deformation. The simplified model assumes that the lithosphere has uniform physical properties, it is denser and much more viscous than the upper mantle, and its penetration below 670 km depth is resisted by a step-like density increase at that level. The primary determinant of the style of deformation is the buoyancy number, F, a ratio of buoyancy stress generated by the mass anomaly in the slab to the stress associated with viscous deformation at a strain rate U_0/L, defined in terms of subduction rate U_0 and slab thickness L. For a small buoyancy number, deformation of the slab is dominated by viscous flexure. For large F, down-dip extension of the slab appears to dominate, and a buckling instability of the slab is observed if there is resistance to penetration of the 670 km level. The transition value of F at which this change in behaviour is observed is about 0.05 for constant viscosity, and about 0.2 for stress-dependent viscosity with a stress versus strain-rate exponent of $n = 3$. With $n = 3$, a boudinage-type instability of the slab is observed for large F. Penetration of the slab below the 670 km level depends on the density contrast between slab and lower mantle. Resisted only by the density difference, the slab may initially penetrate several hundred kilometres below the 670 km level (for plausible density parameters) before a buckling instability causes this part of the slab to rotate and ascend. Comparison of the deforming slab geometry and stress field with seismicity distribution and tomographic images from the Tonga subduction zone suggests that the effective buoyancy number F for this slab is approximately equal to the transition value that we determined experimentally. We use this constraint to estimate average rheological parameters for the Tonga slab which, when compared with published creep deformation laws for olivine, are consistent with the average temperature of the slab being about 0.4 to 0.45 times the melting temperature, based on constitutive laws for olivine. At shallow depths (< 100 km) these temperatures correspond to around 590°C for wet olivine or around 700°C for dry olivine.

Key words: deformation, dynamics, oceanic lithosphere, rheology, subduction.

INTRODUCTION

The key signature of subducted oceanic lithosphere is the Wadati–Benioff zone, the zone of seismicity that traces the descent of the lithospheric slab through the upper mantle. The earthquake locations show that, throughout the descent, the slab generally undergoes relatively large seismic and (by implication) aseismic deformation. The aims of this paper are to test the idea that deformation of the subducted slab results from a balance between the negative buoyancy of the slab and external resistive stress on the surfaces of the slab, to place constraints on the effective rheological parameters of the

* Now at: Department of Earth Sciences, Monash University, Clayton VIC 3168, Australia.

deforming slab, and to examine the effect of a density contrast at the 670 km level on the internal deformation of the slab.

In this conceptual model the slab is defined by its rheological properties. The subducted oceanic lithosphere is assumed much stronger than the upper mantle through which it descends. The slab is bounded by an upper surface, previously the seafloor, and a lower surface defined by some nominal contour of a rheological parameter that represents the mantle's resistance to deformation: for example, it could represent a discontinuity in the rheological parameter caused by an increase in the degree of partial melt or a decrease in water content from lithosphere to asthenosphere (Hirth & Kohlstedt 1996).

Several distinct types of seismically derived data bear on this problem, as reviewed by Lay (1994). First, the location of earthquake epicentres in Wadati–Benioff zones provides a map of where the slab is (e.g. Isacks & Barazangi 1977; Giardini & Woodhouse 1984; Fischer, Creager & Jordan 1991) and where deformation is occurring. The complex structure of the Tonga slab was revealed in considerable detail by the careful relocation of thousands of events by Giardini & Woodhouse (1984).

Second, earthquake focal mechanisms show that the orientation of stress within the subducted slab is often in down-dip extension in the upper part of the subducted slab, and in down-dip compression in the deeper part of the slab towards 670 km (Isacks & Molnar 1969; Vassiliou 1984; Apperson & Frolich 1987). Analyses of principal directions of moment tensors in the Tonga slab show down-dip compression between the surface and 670 km, and a significant component of simple shear in the plane of the slab (Giardini & Woodhouse 1986; Holt 1995) associated with an upper-mantle shear flow in which deep material moves southwards (parallel to strike). A double-planed seismic zone is observed in the upper 200 km of the slab descending beneath the northeastern Japan arc, with distinct focal mechanisms in each plane (Hasegawa, Umino & Takagi 1978). Such double seismic zones have been interpreted in terms of plate flexure, but they are relatively rare and only observed in slabs which are not dominated by tensile or compressive stresses (Fujita & Kanamori 1981).

Earthquake moment tensors can be used to estimate approximate deformation rates within the slab, provided the aseismic deformation is small (Fischer & Jordan 1991; Holt 1995). The Tonga slab is again the best-studied example; it is compressing down-dip and thickening normal to the slab at a rate which varies both down-dip and along-strike (Holt 1995). The average seismic strain rate represents up to 60 per cent of the total relative vertical motion between the surface and the 670 km level (Holt 1995). This magnitude estimate is inversely related to the assumed brittle-layer thickness (15 km). Seismicity gives no indication of the viscous deformation, which is assumed to occur in parallel with the brittle layer with the same strain-rate tensor.

Third, global seismic tomography has given images of seismic velocity in and around subducted slabs (e.g. Zhou & Clayton 1990; van der Hilst *et al.* 1991; Fukao *et al.* 1992; van der Hilst 1995). The magnitude of the *P*-wave velocity anomaly of the slab reaches 10 per cent and is depth-dependent (Anderson 1987; Helffrich, Stein & Wood 1989; Lay 1994); it depends on temperature both explicitly and implicitly through the stability fields of different mineral phases (Anderson 1987). Density is directly related to temperature, and tomography therefore gives an image of the buoyancy forces acting on the slab. The location of the cold slab obtained from tomography may be compared with that obtained from hypocentre locations: they frequently, but not always, coincide. One major example where the two types of image are very different is the subducted slab beneath the Aegean, where the slab imaged tomographically extends to depths of around 600 km but seismicity is absent below 200 km (Wortel & Spakman 1992). The tomographic images also generally have significantly less spatial resolution than the images derived from seismicity; smaller-scale structures are smoothed out and the interpreted images appear simpler.

The lack of recorded seismicity anywhere below about 680 km does not preclude slab penetration into the lower mantle. In particular, the tomographic images appear to show that some subducted slabs penetrate deeper (e.g. Creager & Jordan 1986; Jordan, Lerner-Lam & Creager 1989; van der Hilst *et al.* 1991). The faulting mechanism must be suppressed below this depth, possibly by increasing temperature (Wortel 1982), possibly as a consequence of the polymorphic phase changes associated with this depth level (Kirby 1987). The tomographic images show relatively complex behaviour of the slab at depths of 670 km and below. In some areas the slab levels out at about 670 km; in other areas it appears to descend through the 670 km level to depths of around 1000 km (Zhou 1990; van der Hilst *et al.* 1991; Fukao *et al.* 1992; van der Hilst 1995). Anderson (1987) and Ringwood & Irifune (1988) argued, on the basis of measured mineralogical phase densities, that the subducted slab may find a level of neutral buoyancy at around 670 km, thereby suggesting an explanation as to why some of the slabs might level out at 670 km depth.

Furthermore, some segments of slabs above 670 km may be aseismic and detectable only from tomography through their high-velocity signature (Wortel & Spakman 1992; Ohtaki & Kaneshima 1994), a much more difficult task than simply identifying seismicity. Some isolated deep earthquakes which occur near the 670 km depth, at distances up to 300 km from the Wadati–Benioff zones, may also imply horizontal deflection of a continuous but partially aseismic slab at the 670 km level (Lundgren & Giardini 1994). Alternatively, these isolated deep events have been cited as evidence of detached slab segments (e.g. Barazangi *et al.* 1973; Hamburger & Isacks 1987).

Vertical sections through the Wadati–Benioff zone of Tonga (Giardini & Woodhouse 1984) show that the slab in this region undergoes complex 3-D deformation. This deformation might be interpreted as buckling and tearing of the slab as it descends into the mantle, but it may also be attributable to the time-varying tectonic interaction of the surface plates during subduction (Hamburger & Isacks 1987). In other subduction zones the slab appears to descend smoothly along a curved trajectory in which dip generally increases monotonically (Isacks & Barazangi 1977), attaining a dip of almost 90° in the case of the Marianas slab. The rate of increase of dip with depth is extremely variable from one slab to another. The balance between gravitational torque arising from the negative buoyancy of the slab and the torque caused by viscous resistance to its rotation is perhaps the major control on slab dip angle (Hsui, Tang & Toksoz 1990), although trench migration must also influence the evolution of slab dip (Garfunkel, Anderson & Schubert 1986). The smooth flexing of the plate at subduction was initially described in terms of elastic flexure (Caldwell *et al.* 1976), but the curvature of the slab implies large strains that require some additional component of ductile (or plastic) deformation. The subsequent

reduction in curvature, as the slab descends, shows that this ductile flexing of the slab is later reversed.

Recent measurements of the shear-wave splitting of near-vertical *SKS* waves propagating up through a subducted slab show clear evidence of horizontal anisotropy, with the fast direction almost parallel to the strike of subduction (Vinnik & Kind 1993; Russo & Silver 1994; Gledhill & Gubbins 1996). Perhaps the most probable explanation of this observation is that there is a trench-parallel flow in the mantle beneath the slab (Russo & Silver 1994; Gledhill & Gubbins 1996). This observation suggests that we may be justified in assuming that the subducted slab is only weakly coupled to the convecting mantle beneath; it is the basis for assuming in our calculations that the tractions acting on the surfaces of the slab are small.

Our motivation in calculating quantitative representations of the internal deformation fields of the subducted slab is to explain the dynamical balance which presumably controls the range of observed phenomena described above. Scaled analogue experiments of the subduction process by Griffiths & Turner (1988), Kincaid & Olson (1987), Griffiths, Hackney & van der Hilst (1995) and Guillou-Frottier, Buttles & Olson (1995) have illustrated the modes of deformation of a subducted slab impinging on a fluid interface with a viscosity and/or density increase. These studies have shown the importance of the density contrast and viscosity contrast in governing whether the slab spreads along the interface, sinks through it, or buckles and piles up at the interface. Numerical simulations provide a complementary investigation tool, allowing quantitative estimates of stress and strain rate within the slab. A number of previous studies have attempted to obtain quantitative solutions for the stresses acting within and on the surfaces of an elastic subducted slab, considered separately from the surrounding mantle in which it is embedded (Bird 1978; Wortel & Vlaar 1988; Yoshioka & Wortel 1995; Yoshioka, Yuen & Larsen 1995). In addition there have been many numerical studies of mantle convection phenomena where the subducted slab is treated as part of the convecting mantle system, continuous with its surroundings, but differing because of its greater viscosity and density (e.g. Christensen & Yuen 1984; Gurnis & Hager 1988; Tackley *et al.* 1993; Tao & O'Connell 1993; Gaherty & Hager 1994; Zhong & Gurnis 1995; Davies 1995; Yoshioka *et al.* 1995; King & Ita 1995; Christensen 1996). While the convection approach provides a self-consistent and complete dynamical picture, the slab approach permits the stresses acting within and on the slab to be analysed in greater detail.

Here we follow the approach of separating the slab from the convection within which it is embedded, but assume a viscous rheology, in order to represent the large irreversible strain which must accompany deformation of the subducting slab. Elastic deformation may also be present, but is not considered here. The effect of the rest of the mantle appears through the boundary conditions imposed on the slab. We do not seek to represent the detailed structure of a particular subduction zone because the behaviour and structure of any subduction zone depend on the subduction history, which is generally poorly known. Instead we seek to describe the way in which the important physical parameters control the deformation of the subducted slab.

Laboratory experiments on the deformation of olivine show that the viscous constitutive relationship between stress and strain rate may be either linear or non-linear (Karato, Paterson & Fitzgerald 1986). At low stress levels or high temperatures the deformation mechanism is governed by diffusion, and is linear. At low temperatures and high stress levels olivine is non-Newtonian, and strain rate is approximately proportional to stress raised to the power n, where $n \approx 3$. In either case the coefficient of the constitutive relation incorporates strong temperature dependence via an Arrhenius thermal-activation term. In this paper we examine a homogeneous slab which is either of constant viscosity ($n = 1$), or stress-dependent viscosity ($n = 3$).

METHODS

We assume that deformation is 2-D and plane strain and that the slab is only weakly coupled to the convecting mantle beneath, so that the coupling can be represented in a simple parametric form. Therefore, we solve explicitly for stress and strain rate only in the slab (Fig. 1): the surrounding mantle enters the calculations only through the boundary conditions on the ends of the slab and on its upper and lower surfaces.

We assume that the elastic component of deformation can be neglected and that deformation is governed by a non-linear viscous constitutive relation between deviatoric stress and strain-rate components:

$$\tau_{ij} = 2\eta\dot{\varepsilon}_{ij}, \tag{1}$$

where the effective viscosity η depends on the strain rate parametrized by the second invariant of the strain-rate tensor $\dot{E} = \sqrt{\dot{\varepsilon}_{ij}\dot{\varepsilon}_{ij}}$.

We first investigate the case of a subducted slab with homogeneous properties, neglecting temperature and depth dependence, and write the viscosity as

$$\eta = \eta_0 \left(\frac{L\dot{E}}{U_0} \right)^{(1-n)/n}, \tag{2a}$$

where

$$\eta_0 = \frac{B}{2} \left(\frac{U_0}{L} \right)^{(1-n)/n} \tag{2b}$$

is the viscosity of the material, at a reference strain rate of $\dot{E}_0 = U_0/L$ defined by the velocity scale U_0 (slab velocity) and the length scale L (slab thickness). The parameters B and n (rheological coefficient and exponent) are assumed constant. If $n = 1$ the viscosity is constant. If $n > 1$ strain rate increases as the nth power of the deviatoric stress, and the viscosity is non-Newtonian. Future experiments should examine the dynamical effects of depth- and temperature-dependent viscosity within the slab as it descends into the mantle and reheats, but we aim here to understand the factors that govern deformation of a homogeneous slab.

In the $(x–y)$ plane (Fig. 1), conservation of momentum gives

$$\frac{\partial \tau_{ij}}{\partial x_j} + \frac{\partial P}{\partial x_i} = \delta_{iy}\rho g, \tag{3}$$

where τ_{ij} is the deviatoric stress component, P is pressure, ρ is density, g is gravitational acceleration (in the $-y$ direction) and $\delta_{iy} = 1$ if $i = y$, or else is zero. The total stress component is defined by $\sigma_{ij} = \tau_{ij} + \delta_{ij}P$. We assume also that the medium is incompressible:

$$\dot{\varepsilon}_{xx} + \dot{\varepsilon}_{yy} = 0, \tag{4}$$

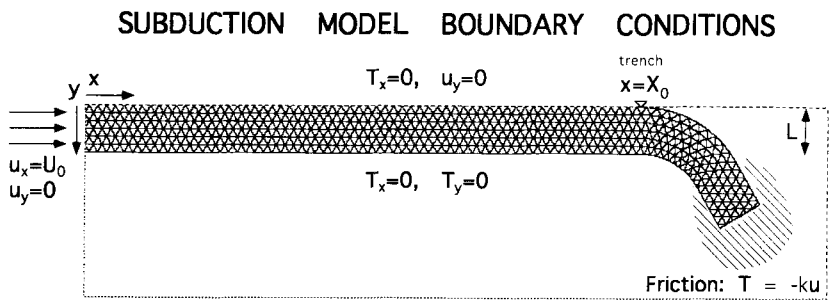

Figure 1. Initial geometry, boundary conditions and finite-element mesh used in the numerical experiments. The boundary condition on the upper surface changes from $u_y = 0$ to $T_y = 0$ as the slab passes the point of subduction at $x = X_0$.

where the strain-rate tensor $\dot{\boldsymbol{\varepsilon}}$ is related to the displacement-rate vector $\mathbf{u}$ by

$$\dot{\varepsilon}_{ij} = \frac{1}{2}\left(\frac{\partial u_i}{\partial x_j} + \frac{\partial u_j}{\partial x_i}\right). \tag{5}$$

We solve the stress balance in the slab for a given set of boundary conditions and internal body force distribution by using the finite-element method applied directly to (3) and (4) (Yamada *et al.* 1975; Huebner 1975). We use triangular elements, quadratic interpolation for velocity, and linear interpolation for pressure. At any given time the stress and strain-rate fields can be derived from the velocity field using (5) and (1). The deformation of the subducted slab is integrated forward in time by advecting each finite-element node using the current velocity field (Houseman & England 1986).

We assume that the slab is dense relative to its surroundings because of thermal contraction. For simplicity, we also assume that its density is uniform and exceeds the density of the mantle through which it descends by a constant amount $\Delta\rho$. In calculating pressures and stresses, and in presenting the results, we subtract from the solutions the lithostatic stress field that results from a stationary fluid medium with stratified background density. Relative to the reference frame provided by the lithostatic stress field, this leaves $\rho = \Delta\rho$ within the slab and $\rho = 0$ in the upper mantle outside the slab.

Increases in density with depth caused by increasing pressure or by phase changes do not affect the deviatoric stress balance if the increases apply equally to the subducted slab and to the background mantle. Although the elevation of the olivine–spinel transition in the cold descending slab should cause an additional localized contribution to the negative buoyancy of the slab just above the 400 km level of this phase transition, we omit this effect to avoid unnecessary complexity. In fact, when the reaction rate of the phase transition is considered, it is unclear whether this transition is actually elevated under conditions of rapid phase equilibrium or depressed because the reaction kinetics are very slow in the cold downgoing olivine of the slab (Goto, Suzuki & Hamaguchi 1987).

Resistance to the slab entering the lower mantle is suggested by the seismic evidence discussed in the Introduction and we therefore include in the model a step-like increase of density of $\Delta\rho_{670}$ at 670 km depth. The lower layer is therefore denser than the slab by $(\Delta\rho_{670} - \Delta\rho)$. Such a density contrast could be caused by the negative Clapeyron slope of the γ-spinel to perovskite phase transition (Anderson 1987; Ito & Takahashi 1989) coupled with the slow thermal response of the descending slab, but the magnitude of any actual density contrast at 670 km is poorly constrained. A compositional density difference between the upper and lower mantle (Jeanloz 1989) is also possible, although recent measurements of thermoelastic properties seem inconsistent with this idea (Jackson & Rigden 1996). We assume no viscosity contrast across the 670 km density interface in the model.

To complete the definition of the problem, we specify boundary and initial conditions as sketched in Fig. 1 for a slab of thickness L. For initial geometry ($t = 0$) we assume that subduction of the slab has already begun, but there is little penetration of the slab into the mantle yet (Fig. 1). The geometry thereafter evolves with time, under the influence of the buoyancy forces and surface tractions. The left-hand end of the slab is assumed embedded in a plate of oceanic lithosphere moving at constant velocity in the $+x$ direction: $u = U_0$, $v = 0$. For $x < X_0$, the nominal subduction point on the surface $y = 0$, the unsubducted plate is constrained to move horizontally by the boundary conditions $\sigma_{xy} = 0$ and $v = 0$ on the upper surface (the seafloor), and $\sigma_{xy} = 0$ and constant normal stress $\sigma_{yy} = -\rho g L$ (equivalent to $\sigma_{yy} = 0$ in the lithostatic reference frame) on the lower surface. We assume that normal (minus lithostatic) and tangential tractions acting on the surfaces of the subducted slab are zero except for a frictional drag on the leading end of the slab. This is justified if the viscosity of the asthenosphere is small compared with that of the slab.

The simplest way to represent a viscous drag on the boundary is by means of a frictional relation:

$$T_i = -k u_i, \tag{6}$$

where T_i is the traction component acting on an external boundary segment of the slab, u_i is the velocity component, and k is a frictional resistance constant, with dimensions of stress divided by velocity. The traction on the boundary is opposite in direction and proportional in magnitude to the velocity. A frictional relation in which displacement rate is proportional to resistive traction is consistent with Stokes-type resistance to the movement of a body through a linear viscous material. In this case k is proportional to the viscosity of the surrounding fluid, and inversely proportional to a characteristic length scale. We assume that most of the frictional resistance is encountered at the end of the slab, as it initially descends through the mantle. Therefore, we set $k = k_0$ on the end of the slab, and require that k is tapered linearly from k_0 to zero over a distance L from the end of the subducted slab. Elsewhere on the subducted part of the slab, the zero traction condition is equivalent to $k = 0$.

The governing equations are made dimensionless by using the length scale L, the velocity scale U_0, the density scale $\Delta\rho$, the viscosity scale η_0, and the stress scale $T_0 = \eta_0 U_0/L$, and (3) becomes:

$$\frac{\partial \tau'_{ij}}{\partial x'_j} + \frac{\partial P'}{\partial x'_i} = \delta_{iy} F \rho', \tag{7}$$

where

$$F = \frac{2Lg\Delta\rho}{B}\left(\frac{L}{U_0}\right)^{1/n}, \tag{8a}$$

and for $n = 1$

$$F = \frac{L^2 g \Delta\rho}{U_0 \eta_0} \tag{8b}$$

is the dimensionless coefficient of the buoyancy term. For Newtonian viscosity, the buoyancy parameter F is the reciprocal of the viscosity parameter Y used in the previous studies of Cruickshank & Munson (1981) and Griffiths & Turner (1988). The dimensionless friction coefficient is then

$$k' = \frac{Lk}{\eta_0} = \frac{2Lk}{B}\left(\frac{U_0}{L}\right)^{(1-n)/n}. \tag{9}$$

Other significant dimensionless variables are the normalized density contrast between the slab and lower mantle, $R = (\Delta\rho - \Delta\rho_{670})/\Delta\rho$, as defined by Kincaid & Olson (1987), and the ratio of the thicknesses of the upper mantle (670 km) to the slab, H_{um}/L.

RESULTS

We carried out a series of experiments to examine the dependence of the slab deformation history on variations of the following parameters: the buoyancy coefficient F, the friction coefficient k'_0, the relative density contrast at 670 km R and the rheological exponent n. We assume a length scale $L = 80$ km and velocity scale $U_0 = 80$ mm yr^{-1}, so the time unit for dimensionalization is $L/U_0 = 1$ Myr, and fix the ratio $H_{um}/L = 8.375$. We use dimensional units in describing the results, but note that time (and other derived units) must be rescaled if L or U_0 is changed.

Deformation history: reference experiment

We first describe the evolution of the system for a reference experiment with $n = 1$, $F = 0.05$, $R = -1$, and $k'_0 = 0.02$ (Fig. 2). In the initial stage of slab descent, the negative buoyancy of the slab dominates its evolution. The unsubducted end of the slab moves at a constant velocity of U_0 and the end of the slab descends at approximately the same velocity (extension in the slab is minor). As the slab passes the subduction point, it is no longer constrained to lie on the surface and is pulled downwards by the weight of the previously subducted slab (Fig. 2a). The deformation may be described locally as a curvature or flexure of the slab but, since this is a viscous flexure rather than an elastic flexure, very large flexural strains may be generated without the extreme bending moments which would be required for elastic flexure.

The body force which causes the slab to bend after it is first subducted also causes the deformation to be reversed by straightening the slab after it has descended below about 150 km. Reversal of the flexure is not complete because the relevant bending moment is small towards the lower end of the slab, or when the dip of the slab approaches 90°. Frictional resistance at the leading end of the slab also prevents complete recovery. Dip increases smoothly from the subduction point to rapidly approach, and exceed, 90°. Below the zone of flexure, a vertical dip is of course the preferred solution for a long slab influenced only by gravity. The dip goes beyond vertical usually before the flexure is completely reversed; a similar effect can be observed with honey pouring off the edge of a spoon.

Subduction continues in this mode until the end of the slab descends below 670 km (Fig. 2b). Until this time the total body force acting on the slab increases in proportion to the length of the descending slab, so the net down-dip extensional stress in the upper part of the slab increases also. After the leading edge of the slab descends below 670 km, however, it becomes positively buoyant because of the relatively greater density of the lower mantle. Although resisted by the density contrast, it continues to descend, reaching a depth of 932 km (at $t = 8.65$ Myr) before beginning to rise again. The continued descent is not caused by the inertia of the slab (which is negligible in such an extremely viscous fluid). The weight of the subducted slab in the upper 670 km is partly balanced by viscous stresses causing deformation within the slab and partly balanced by the upward buoyancy of the slab below 670 km.

At this stage (Fig. 2c) the almost vertical slab is under considerable down-dip compression due to the negative buoyancy above and the positive buoyancy below. The consequence of this compression is a buckling instability, the progress of which is observed in the final three frames of Fig. 2. Following the buckling instability, that part of the slab which descended to 932 km rapidly comes up again to its level of neutral buoyancy at around 670 km. A focus of extreme slab curvature occurs just above the 670 km level, as the slab folds over on itself. The experiment is stopped at the point where the slab is completely folded over on itself because of computational limitations which are not of physical significance. Because the buckling instability grows from whatever non-zero curvature may be present in the subducted slab, the slab at 670 km may buckle with concave curvature either on the crustal side (as in Fig. 2) or on the asthenospheric side.

The deformation of the slab is plane strain in these experiments; at any point the strain-rate field is described by a magnitude, $\dot{\varepsilon}_{11} = -\dot{\varepsilon}_{22}$, and an orientation, θ, of the principal strain-rate axes. In describing the results, we show the orientation of the principal compressive strain-rate axis (Fig. 3) and contours of the magnitude of the principal strain rate (Fig. 2); the extensional axis is orthogonal to the compressional axis and has the same magnitude. The maximum shear strain rate has the same magnitude and occurs on planes at 45° to the direction θ.

Before the slab reaches the 670 km level, we see that the weight of the slab causes extensional stress in the vertical part of the slab, and the predominant stress orientation is down-dip extension (Fig. 3a). Later in the experiment when the end of the slab has penetrated below 670 km (Fig. 3b), the lower half of the slab is predominantly in down-dip compression, while the upper half remains partly in down-dip extension. A transition in stress orientation occurs across a neutral surface which crosses the near-vertical slab at an oblique angle (Fig. 3b). Near the end of the experiment the strain-rate orientations are dominated by the flexural deformation of the

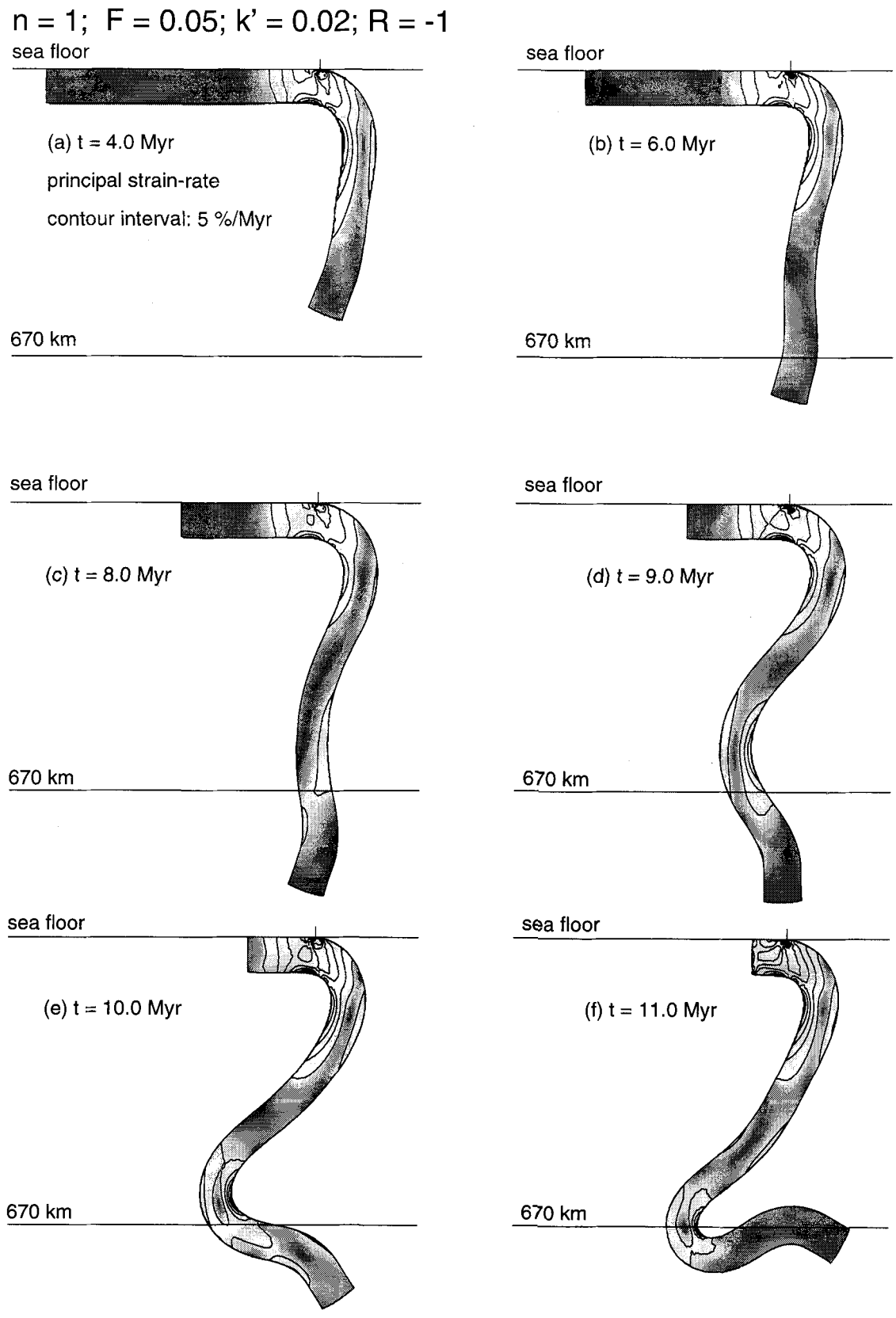

Figure 2. Geometry of the subducted slab for the experiment with $n = 1$, $F = 0.05$, $k_0' = 0.02$ and $R = -1$ at successive times after the initial condition shown in Fig. 1. Superimposed on the slab drawings are contours of maximum shear strain rate. The contour interval is 5 per cent Myr^{-1} (or 0.05 in units of U_0/L) and regions of low strain rate ($0 \leq \dot{\varepsilon} \leq 5$ per cent Myr^{-1}) are the darkest shade of grey. High-strain-rate regions generally indicate where the slab is flexing.

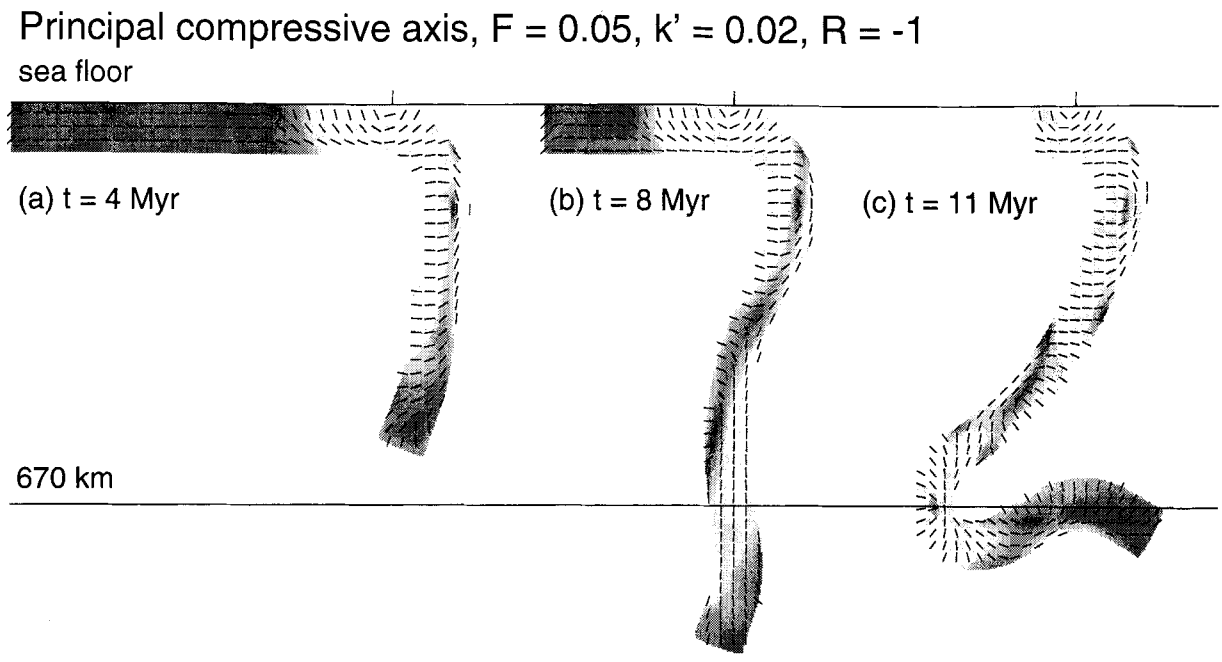

Figure 3. Principal strain-rate orientations (compressive) at (a) $t = 4$ Myr, (b) $t = 8$ Myr, and (c) $t = 11$ Myr, in the same experiment shown in Fig. 2 ($n = 1$, $F = 0.05$, $k_0' = 0.02$ and $R = -1$). The principal direction arrows all have the same length, and are superimposed on an image of maximum shear-strain rate in which regions of low strain rate ($0 \leq \dot{\varepsilon} \leq 0.03$ per cent Myr^{-1}) are shaded grey. In the dark regions the direction of the axes is poorly constrained because the difference between the two principal strain-rate axes is small.

plate, but the basic pattern of vertical extension in the upper part of the slab and vertical compression at greater depths is partly preserved (Fig. 3c).

The low-strain-rate neutral plane running through the slab (shaded grey in Fig. 3b) is diagnostic of flexural deformation. With viscous flexure the orientations of the principal strain-rate axes do not depend directly on the curvature, but rather on the direction in which the curvature is changing. If the curvature of the surface is becoming more convex (or less concave) the compressional axis is perpendicular to that surface; similarly, the opposite surface becoming less convex (or more concave) has a compressional axis parallel to the surface. In the upper 200 km of Fig. 3(c), we see that the upper (crustal) surface of the plate is everywhere convex, yet the direction of compression near this surface changes with depth. In the upper 50 km or so, compression is perpendicular to the surface as the plate is flexed while, below about 50 km, the compression is parallel to the surface as the plate is straightened. The flexural alignment of stress axes is also clearly evident in Fig. 3(c) where the slab is undergoing extreme bending at about 670 km.

Strain-rate magnitudes are small in the end of the slab near the 670 km level (Fig. 3c), but the orientations of the axes are explained by the continuing unflexing of this part of the slab as it relaxes back to horizontal alignment, the situation in which its gravitational potential energy is minimized.

Influence of the density contrast at 670 km

The growth of the buckling instability in these experiments requires a density contrast $R < 0$ at 670 km. This density contrast creates the down-dip compression which causes the buckling to occur. We may ask how the growth of the instability is influenced by the magnitude of this density contrast. If R is increased from -0.1 to -0.5, with other parameters unchanged, the same buckling instability is observed, but it is predictably slower to develop. With $R = -0.5$, the slab develops a 90° bend at the 670 km level (as in Fig. 2e), but this stage is reached at about $t = 11$ Myr instead of $t = 10$ Myr and the end of the slab reaches a depth of 1025 km (at $t = 9.75$ Myr) before it starts to come up again. If R is increased further to -0.25, the slab penetrates to 1167 km (at $t = 11.65$ Myr) before the buckling instability causes it to come up again. With $R = -0.25$, the 90° bend is not attained before the end of the experiment at $t = 12$ Myr, but the slab below 670 km is clearly moving upwards.

In each of these experiments the observed evolution of slab geometry is qualitatively similar to that shown in Fig. 2. When R is closer to zero, the evident change is that the end of the slab penetrates further below the 670 km level and comes back up more slowly. The rate at which it comes back up depends on the rate of growth of the buckling instability, which is positively correlated with the density difference and the length of slab below 670 km, and inversely correlated with the viscosity of the slab.

Influence of friction on the end of the slab

The frictional boundary condition on the end of the slab is only a rough approximation to the viscous resistive stresses that would act on a slab descending through a viscous mantle layer. Nevertheless, we ask how the reference solution is affected by changing the magnitude of the frictional parameter if the distribution of friction is unchanged. With other parameters unchanged, we repeated the reference experiment with $k_0' = 0.005$, 0.01, 0.05 and 0.1. In these experiments we found that the buckling instability observed with the reference experiment ($k_0' = 0.02$, Fig. 2) was also observed (though

slightly modified) with $k'_0 = 0.005$ (Fig. 4a), and $k'_0 = 0.05$. The maximum depth reached is inversely correlated with k'_0, varying from 958 km for $k'_0 = 0.005$, to 932 km for $k'_0 = 0.02$, to 825 km for $k'_0 = 0.05$. At the end of the experiments there is significantly greater overall elongation of the slab (of the order of 5 per cent) with $k'_0 = 0.005$, compared with $k'_0 = 0.05$, but the final geometry is surprisingly similar in all three experiments with $k'_0 = 0.005$, 0.02 and 0.05.

Somewhat different behaviour was observed with the other two experiments in this series. With $k'_0 = 0.01$ and other parameters as above, the end of the slab rotated clockwise instead of anticlockwise after penetrating the 670 km level (Fig. 4b). Instead of buckling, that part of the slab between 0 and 670 km depth remains relatively straight and almost vertical. As the slab hits the density interface it turns over and continues horizontally in the negative x-direction, in much the same way as if the slab were the thermal boundary layer of a convection cell. The viscous flexing and unflexing of the slab which occurs at the point of subduction is thus repeated at 670 km. We refer to this type of slab geometry (Fig. 4b) as slab rollover, to distinguish it from the slab-buckling geometry depicted in Figs 2 and 4(a).

It is somewhat unexpected that the experiment with $k'_0 = 0.01$ shows slab rollover (Fig. 4b), whereas either doubling or halving the friction coefficient results in slab buckling (Figs 2 and 4a). We conclude from this observation that either type of behaviour is possible for a slab descending from a fixed subduction zone, but whether the end of the slab is rotated clockwise (rollover) or anticlockwise (buckling) depends on the detail of the slab-curvature distribution as the slab reaches its point of maximum descent. In this experiment the slab reached a depth of 900 km, some 40 km less than would have been expected with the buckling mechanism.

In a final experiment in this series, we set $k'_0 = 0.1$, with other parameters as before, and observe another style of deformation. In this case the leading edge of the slab meets considerable resistance, and the end of the slab rolls over in a clockwise sense as the slab descends through the upper mantle (Fig. 4c). The leading edge makes a tight hook, which presents a new zero-friction leading edge (as defined by the boundary conditions). This particular style of deformation thus appears to be an artefact of the boundary conditions we use. We conclude that for a given buoyancy factor F, there is a maximum k'_0 that is physically consistent with the boundary condition formulation, and experiments in which k'_0 is above this maximum value result in the formation of this hook at the end of the slab, and are invalid. On the other hand, we find that if k'_0 is much less than this maximum value then the solutions we obtain are almost independent of the actual value of k'_0.

Influence of the buoyancy parameter F

From eq. (7) the buoyancy parameter F is the principal control on the relative importance of buoyancy forces and internal viscous stress within the plate. If F is increased, either by increasing the buoyancy force (through $\Delta\rho$, g or L), or by decreasing the magnitude of viscous stress (through η_0 or U_0), gravitational stress becomes a more important factor relative to surface tractions. With the rheological exponent $n = 1$ and density contrast $R = -1$, we completed experiments with $0.005 \leq F \leq 0.2$ (Fig. 5). The rheological constant η_0 is the most uncertain parameter appearing in expressions (8) and (9) for F and k' and we conduct a series of experiments varying F and k' in proportion, effectively varying η_0. Further experiments with a range of k'_0 values for each value of F show that the observed deformation depends only weakly on k'_0 if k'_0 is sufficiently small.

To examine values of the buoyancy factor F less than that of the reference experiment, we used $F = 0.02$ (with $k'_0 = 0.002$ to $k'_0 = 0.02$) and $F = 0.005$ (with $k'_0 = 0.0005$ to $k'_0 = 0.02$). The deformation of the slab for both sets of experiments is dominated by viscous flexural bending rather than shortening or elongation. For small F the outline of the slab forms a smooth arc as it is pulled down into the mantle (Figs 5a and b). The slab steepens more rapidly with larger F. The effective buoyancy force is significantly less than in the reference experiment, so the curvature induced in the slab at subduction

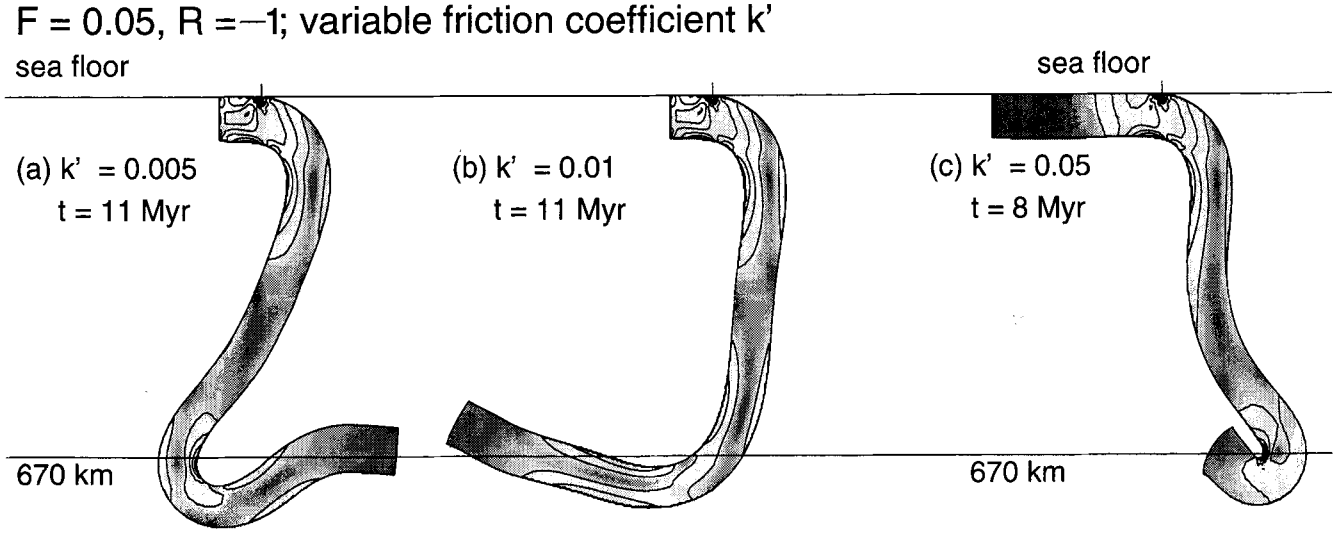

Figure 4. Principal strain-rate images for three experiments with $n = 1$, $F = 0.05$, $R = -1$, and variable friction coefficient. With $k'_0 = 0.005$ (a), the buckling instability occurs; with $k'_0 = 0.01$ (b), slab rollover occurs; with $k'_0 = 0.05$ (c), the high friction coefficient is inconsistent with other boundary conditions and an artificial slab hook is generated. Contour intervals and shading are as in Fig. 2.

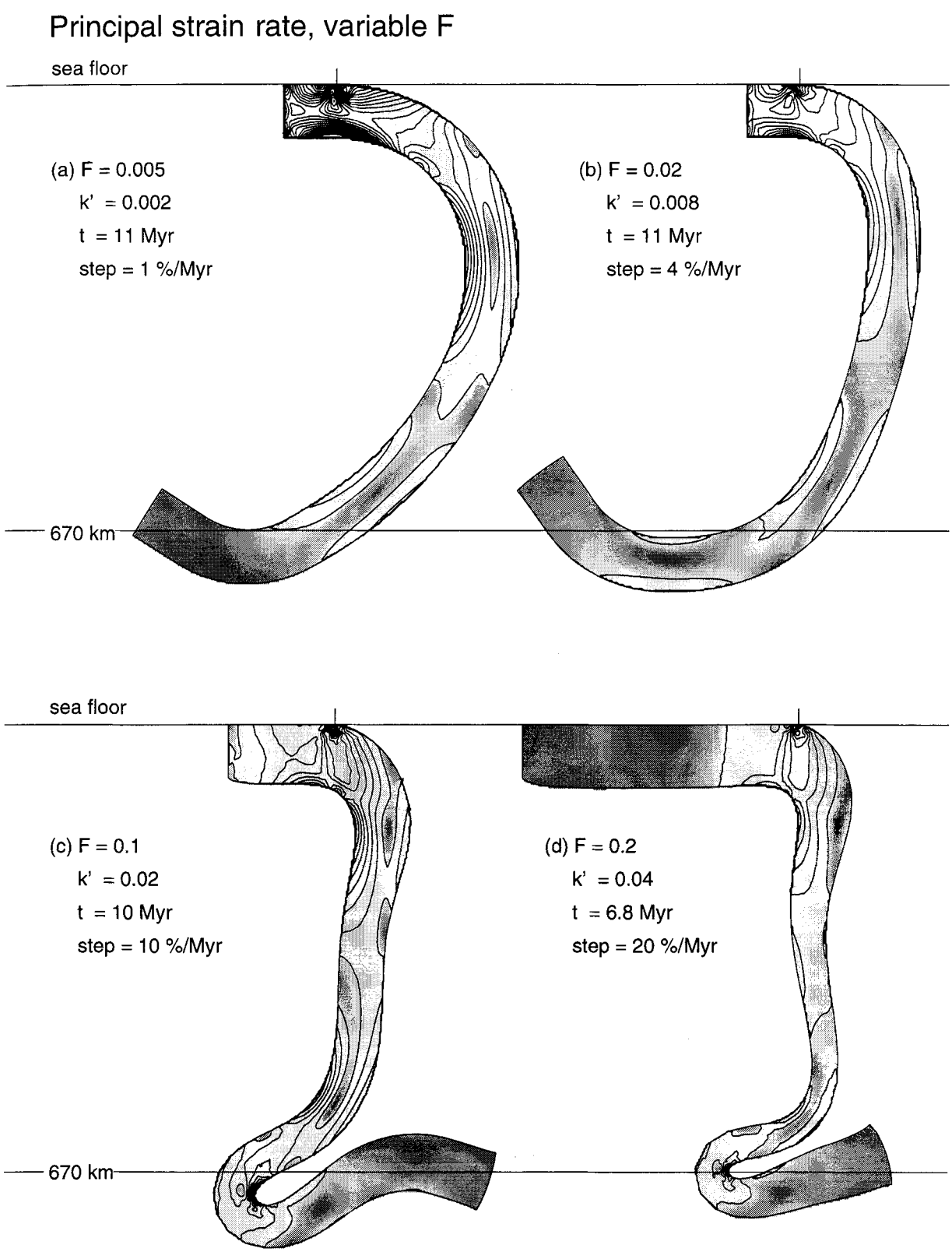

Figure 5. Geometry and principal strain-rate contours of the subducted slab for four different experiments with increasing F value. With $F =$ 0.005 (a) and $F = 0.02$ (b), viscous flexure dominates. With $F = 0.1$ (c) and 0.2 (d), down-dip extension dominates. Friction coefficient k_0', elapsed time t, and contour interval (step) are shown on each frame. In each case the zone between zero strain rate and the first contour level is shaded grey.

is not quickly reversed. In each case the end segment of the slab retains most of its initial curvature. As the curved leading edge of the slab hits the density discontinuity at 670 km it is oriented favourably to roll clockwise and run back along the 670 km level, in the opposite direction to the surface plate velocity. For each of these small-F experiments we found that, instead of buckling, the slab rolls over when it hits the density interface at 670 km.

We found for $F = 0.02$ that k_0' should be less than about 0.01 to avoid the hooked leading-edge artefact (e.g. Fig. 4c). For $F = 0.005$, the maximum value of k_0' is about 0.002. In all the other experiments with $F = 0.02$ or 0.005, the curvature of the final slab shape is similar, as shown in Figs 5(a) and (b), and does not depend strongly on the magnitude of k_0'. Curvature of the subducted slab is distributed more uniformly along its length compared with the reference experiment. Maximum flexural shear strain rates are observed in the plate at the subduction point and secondary maxima at depths of 250 to 300 km. Third, and even fourth, local maxima in the bending moment may occur just above and just below the 670 km level, respectively (Figs 5a and b). The neutral surface of the viscous flexing slab is clearly evident in all of the small-F experiments.

For values of the buoyancy factor F greater than that of the reference experiment, we used $F = 0.1$ (with $k_0' = 0.01$, 0.02 and 0.04) and $F = 0.2$ (with $k_0' = 0.02$, 0.04 and 0.08). Gravity clearly exerts a much stronger influence in these experiments (Figs 5c and d). Elongation and thinning of the slab caused by down-dip extension is evident with $F = 0.1$ (Fig. 5c) and extreme with $F = 0.2$ (Fig. 5d). The radius of curvature of the flexing slab at the subduction point decreases with increasing F. In each of these experiments the rate of increase of slab dip with depth is much greater than in the low buoyancy-number experiments, and a slab dip of approximately 90° is attained at a depth of 150 to 200 km as the slab straightens out again under the influence of a relatively stronger gravitational stress. Slab dip is nearly vertical over most of the length of the subducted slab, until it hits the density interface at 670 km.

We observe slab buckling in each of the three experiments with $F = 0.1$. The two experiments with greater friction coefficient ($k_0' = 0.02$ and 0.04) are very similar; the end of the slab rotates anticlockwise so that the leading end of the slab points in the $+x$ direction as the material above is folded over (Fig. 5c). In the third experiment ($k_0' = 0.01$), the end of the slab rotates clockwise so that the leading end of the slab points in the $-x$ direction. The folding of the deeper part of the slab occurs almost as the mirror image of the first two experiments. In these three experiments, the maximum depth reached by the slab is inversely correlated with k_0': 892 km for $k_0' = 0.01$, 878 km for $k_0' = 0.02$ and 800 km for $k_0' = 0.04$.

The three experiments with $F = 0.2$ ($k_0' = 0.02$, 0.04 and 0.08) showed a similar change in polarity of the buckling mode as k_0' was increased. The experiment with the smallest friction coefficient again shows the leading end of the slab rotating clockwise whereas the other two experiments show it rotating anticlockwise (Fig. 5d). After the initial buckling instability has occurred, the clockwise and anticlockwise solutions are almost mirror images below the subduction point. The maximum depth reached by the slab is also inversely correlated with k_0' for $F = 0.2$: 825 km, 784 km and 753 km for $k_0' = 0.02$, 0.04 and 0.08, respectively. Just above the 670 km level, the slab is thinned by down-dip extension to between 50 and 60 per cent of its original thickness in these experiments with $F = 0.2$.

At small F (Figs 6a and b) the stress field is dominated by flexure, while at large F (Figs 6c and d) it is increasingly dominated by down-dip extension. For $F = 0.005$ the flexing and unflexing of the slab are indicated by the 90° rotation of stress direction across the neutral plane outlined in grey (Fig. 6a). Near the subduction point the slab is flexing to subduct, at mid-depths (300–400 km) it is straightening out, and just above 670 km it bends again as it hits the density discontinuity. A similar pattern is observed for $F = 0.02$ (Fig. 6b), the most notable difference being that the neutral surface moves slightly towards the upper (crustal) surface of the slab, because of greater down-dip extension.

For $F = 0.1$ (Fig. 6c), down-dip extension dominates the slab stress field across most of the upper mantle, although there are significant zones of compression caused by flexure on the crustal side in the upper 300 km, and on the asthenospheric side in the lower 300 km. For $F = 0.2$ (Fig. 6d) the down-dip extension dominates to the extent that the neutral plane is almost forced out of the slab throughout the upper mantle. Flexure remains the dominant aspect only in those parts of the slab near the subduction point, and in the tight fold near 670 km.

Experiments with retrograde trench migration

In all the experiments described so far the subduction point was stationary relative to the mantle beneath. In many actual subduction zones, however, we observe that the point of subduction moves with respect to the mantle. Such trench migration is generally retrograde, and is often related to back-arc extension behind the subduction zone, although the rate of trench migration is usually small compared with the subducting plate velocity. To investigate the effect of retrograde trench migration, we ran a series of experiments in which the subduction point moves in the opposite direction to the plate at a quarter of the speed of the subducting plate, effectively feeding the slab into the mantle 25 per cent faster. With $F = 0.02$, $k_0' = 0.002$, and other parameters as in Fig. 5(b), the subducted slab deforms to the same shape illustrated in Fig. 5(b), but the final configuration is simply translated to the left by the same distance as the trench. With $F = 0.5$, $k_0' = 0.005$ or 0.02, and other parameters as shown in Figs 2 and 3, we also observed that the migration of the trench did not have a significant effect on the final shape of the subducted slab. The same final shapes shown in Figs 2(f) and 3(a) were reproduced with minor changes except that the entire slab was shifted to the left by the distance of trench migration.

With increasing F the effect of trench migration is more significant. Comparing Fig. 7 ($F = 0.1$ and $k_0' = 0.01$) with Fig. 5(c) ($F = 0.1$ and $k_0' = 0.02$), we see that the buckling instability is modified as the subduction point moves to the left relative to the subducted plate. The leading end of the slab levels out at around 670 km, and continues to move in the $+x$ direction, while the vertical part of the slab is moving to the left with the subduction point. The resulting geometry in which the subducted slab spreads out on top of the density interface at 670 km is in contrast to the sharp folding of the slab shown in Fig. 5(c). At $t = 9$ Myr in this experiment the velocity is generally parallel to the surface of the slab (Fig. 7b), indicating that an almost steady-state shape for the subducted

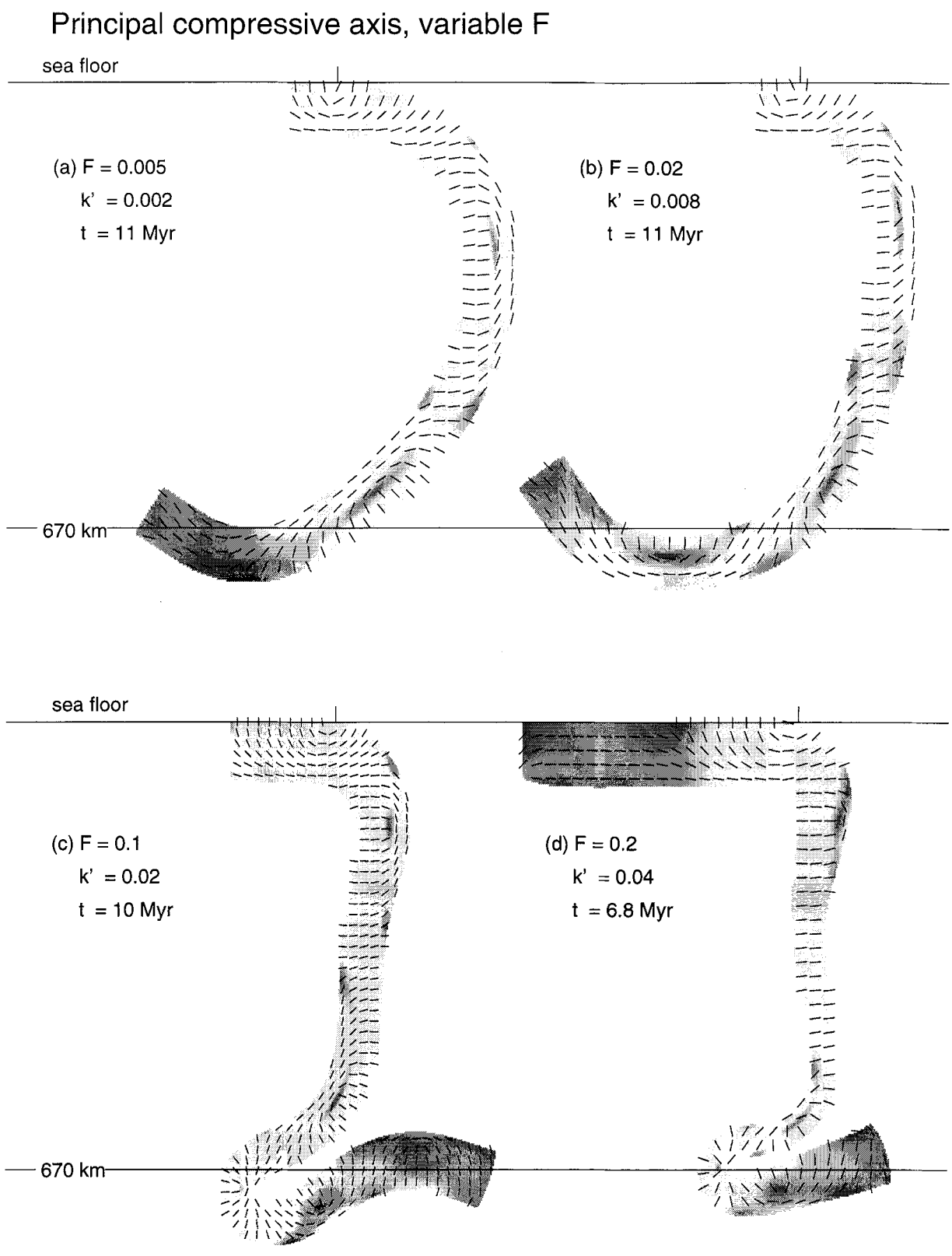

Figure 6. Principal compressive stress directions within the slab for the same solutions shown in Fig. 5. Plotting conventions are as in Fig. 3. Regions in which the principal strain rate is less than (a) 0.4 per cent Myr^{-1}, (b) 1.4 per cent Myr^{-1}, (c) 4.0 per cent Myr^{-1} and (d) 7.0 per cent Myr^{-1} are shaded grey.

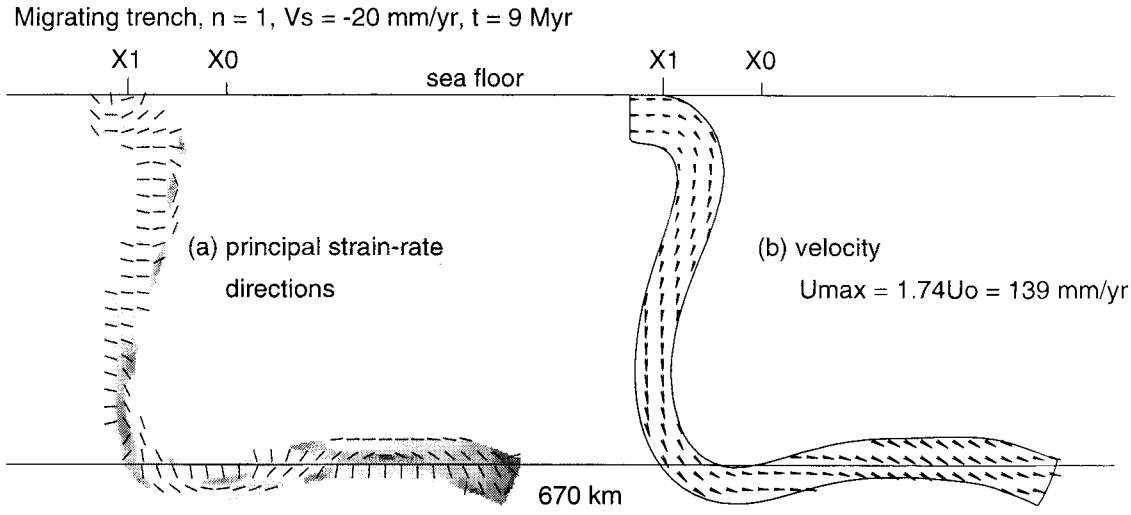

Figure 7. Final geometry of the slab ($t = 9$ Myr) in an experiment with $n = 1$, and $F = 0.1$, when the overriding plate moves to the left at a rate of 20 mm yr^{-1} ($0.25U_0$), while the slab moves to the right at a rate of 80 mm yr^{-1} (U_0). Principal strain-rate directions (a) are shown with shading as in Fig. 6(b), instantaneous velocity vectors (b) are scaled to a maximum velocity of 139 mm yr^{-1} ($1.74U_0$). The trench is originally at $x = X_0$ and moves to $x = X_1$ during the experiment.

slab has been attained. The increase in velocity with depth in the slab indicates down-dip elongation of the slab, consistent with the principal strain-rate directions (Fig. 7a) and thinning of the slab with depth.

The above experiments with a migrating trench must be interpreted with caution, because the boundary conditions we use here imply that the vertical slab can move freely in the horizontal direction. In reality such movement requires the displacement of a large volume of mantle on both sides of the slab, implying large normal tractions on the surface of the slab.

Stress-dependent viscosity, $n = 3$

With $n = 3$ the dependence of F on U_0 and L is reduced (for example, a factor of 8 increase in U_0 only causes F to be halved). Experiments with a range of F values (Fig. 8) show the same general trend of deformation dominated by viscous flexure for small F and down-dip extension and buckling for large F. In general, slab deformation is more sensitive to the value of F for $n = 3$ than $n = 1$. The cases $n = 3$, $F = 0.2$ (Fig. 8a) and $n = 1$, $F = 0.05$ (Fig. 2) have a similar style of deformation, in which flexure dominates but the effect of down-dip extension can just be perceived as a subtle variation in slab thickness.

A subtle but significant difference in the style of flexural deformation from $n = 1$ to $n = 3$ is observed in comparing Figs 2(e) and 8(a). The buckling deformation with $n = 1$ is more evently distributed along the length of subducted slab. Because of the stress-dependent viscosity, slab flexure with $n = 3$ is necessarily more concentrated in the hinge zones where the stress is maximum, and these zones are separated by relatively undeforming segments of slab (the grey zones in Fig. 8a). The neutral surface takes on a greater significance with $n = 3$, because the low stress values near the surface imply a high-viscosity core to the slab. The slab buckling that occurs when the end of the slab sinks below 670 km is apparently delayed with $n = 3$, so that the slab penetrates to a greater depth and then buckling occurs suddenly and rapidly, with the slab flexing just above 670 km. With $n = 3$, $F = 0.2$ and $R = -1$, the maximum slab penetration depth is 969 km (with $k_0' = 0.02$) or 958 km (with $k_0' = 0.01$), compared with the depth of 932 km in the $n = 1$ reference experiment.

With $n = 3$ and $F = 0.05$ (Fig. 8b) the slab undergoes flexural deformation with little change in thickness, similar to that observed at small F and $n = 1$ (Fig. 5a,b). For $n = 3$ and $F = 0.5$ the buoyancy force completely dominates, and a strong necking or boudinage instability develops at about 300 km depth (Fig. 8c) because the slab is too weak to support the weight of the previously subducted slab. The value of F at which down-dip extensional strain takes over from viscous flexure is 2 to 4 times that found in the $n = 1$ experiments.

COMPARISON TO OTHER EXPERIMENTS

The onset of buckling in a viscous jet or slab was previously studied by Cruickshank & Munson (1981) and Griffiths & Turner (1988). They showed that the onset of buckling in a vertical sheet with no initial asymmetry occurs whenever the length of the sheet exceeds a critical height which is typically of the order of 1 to 3 times the layer thickness. They also found that the buoyancy parameter has only a small effect on the critical height, but has a strong effect on the frequency of buckling for a steady-state flow, once the critical height is exceeded. In contrast, we found that the style of deformation of the slab in our experiments depends strongly on F, although we did not vary the height to thickness ratio H_{um}/L. Our experiments differ from the earlier ones because the plate is initially horizontal rather than vertical and because we are limited to calculations that examine only the transient behaviour that is associated with the slab initially impinging on the density interface. Our conclusions do not therefore contradict those earlier studies, but they do indicate more complex behaviour than when the subducted slab is initially vertical.

The experiments of Kincaid & Olson (1987) demonstrate the critical role of the density-contrast parameter R in determining the depth of penetration at the 670 km level. Our

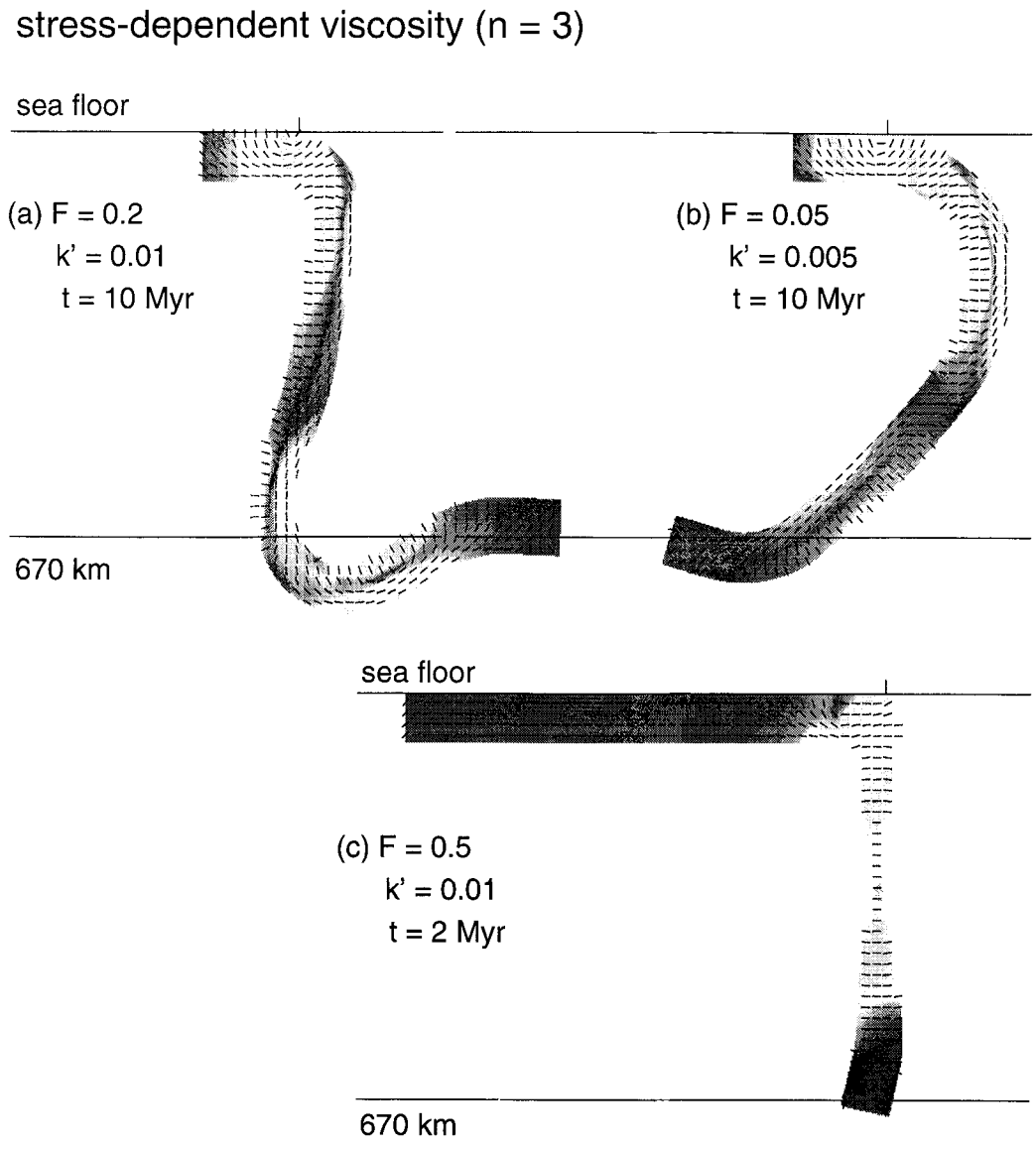

Figure 8. Geometry and maximum principal stress directions for three experiments with stress-dependent viscosity ($n = 3$) and (a) $F = 0.2$, (b) $F = 0.05$ and (c) $F = 0.5$. Friction coefficient k_0' and elapsed time t are shown on each frame. Grey shading is applied to those regions in which the principal strain rate is less than (a) 3 per cent Myr^{-1}, (b) 0.5 per cent Myr^{-1} and (c) 2 per cent Myr^{-1}.

experiments fall entirely in the range $R < -0.2$, for which they found that slab penetration into the lower mantle was small, but their experiments included an order of magnitude viscosity step from upper- to lower-mantle layer, which slows penetration of the slab into the lower mantle. Their experiments appear to be entirely in the low-F regime, but lack of a velocity scale or timescale in their paper does not permit the relevant buoyancy factors F to be estimated. Guillou-Frottier *et al.* (1995) used values of the buoyancy ratio less than about 0.0003 in their experiments, entirely within our low-F regime. They also included a large viscosity step from upper layer to lower, and showed a range of complex interactions between the slab and this interface. Their upper-layer slabs are qualitatively similar to our upper-layer slabs for small F, although they showed that the slab may buckle into a large folded pile in the lower layer if subduction continues for a long period.

The experiments by Griffiths *et al.* (1995), Guillou-Frottier *et al.* (1995) and Christensen (1996) also showed the influence of trench migration on slab dip. Compared to our trench-migration experiments, in which the slab-normal tractions that arise because of the fluid dynamical pressure difference between the two mantle reservoirs on either side of the slab are omitted, these earlier experiments illustrate the effect of this pressure difference in determining slab dip (Garfunkel *et al.* 1986).

IMPLICATIONS FOR SLAB RHEOLOGY

The most uncertain parameter in the expression for F (eqs 8a and b) is the viscosity η_0 (for $n = 1$), or the rheological coefficient B (for $n > 1$). We now use observations of subducted slab geometry and stress in the Earth to estimate F, and hence η_0 or B. The complex morphology of the Tonga–Kermadec slab (Giardini & Woodhouse 1984; van der Hilst, 1995) strongly suggests that some form of slab buckling has occurred and is still occurring. The buckling instability only occurs for F greater than some critical value ($F_{min} \approx 0.05$ for $n = 1$,

$F_{min} \approx 0.2$ for $n = 3$). The relevant buoyancy number for the Tonga slab should therefore exceed the critical value. A second important diagnostic is the orientation of the principal compressive stress determined from earthquake mechanism studies. In all subducted slabs, deep events tend to show down-dip compression (Isacks & Molnar 1969; Apperson & Frolich 1987). The experiments only show significant down-dip compression for values of F less than $F_{max} \approx 4F_{min}$.

Down-dip compression is observed in our experiments in two different circumstances: if the slab is flexing or unflexing, we see compression on one side of the slab. Second, if the slab's descent meets resistance caused by the density step at 670 km, the deeper part of the slab may be entirely in compression. The latter is most evident when the slab has penetrated the 670 km level and is yet to buckle (e.g. Fig. 3b). If F is larger than about 0.2 ($n = 1$) or 0.5 ($n = 3$), we see that the region of down-dip compression is restricted to within 100–200 km above the 670 km level and is associated with flexure.

Taken together, the inferences from slab geometry and stress orientation seem consistent with this model (at least for the Tonga subduction zone) only if F is rather tightly constrained to have a magnitude of about 0.1 (if $n = 1$), or 0.2 (if $n = 3$). We may then solve eq. (8b) using $g = 10\ \mathrm{m\ s^{-2}}$, $L = 80$ km, $\Delta\rho = 80\ \mathrm{kg\ m^{-3}}$ and $U_0 = 65\ \mathrm{mm\ yr^{-1}}$, to obtain, for $n = 1$, an effective viscosity of the subducted slab $\eta_0 = 2.5 \times 10^{22}$ Pa s. This value represents a volumetric average over the subducted slab and is about 200 times greater than the upper mantle viscosity of $(1–2) \times 10^{20}$ Pa s (Nakada & Lambeck 1989), but only about 2.5 times greater than the lower-mantle viscosity estimated by the same authors.

Alternatively, for stress-dependent viscosity ($n > 1$) we can use the rheological coefficient B, obtained by solving eq. (8a), in conjunction with rheological constitutive relations measured in laboratory experiments, to estimate a slab temperature. We assume a creep law of the form

$$\dot{\varepsilon} = A(\sigma_1 - \sigma_3)^n \exp\left(-a\frac{T_m}{T}\right), \tag{10}$$

where σ_1 and σ_3 are the maximum and minimum stresses, T is temperature, T_m is the melting temperature (both in Kelvins), and A and n are experimentally determined constants. The parameter $a = H/(RT_m)$, where H is the activation enthalpy and R ($= 8.314\ \mathrm{J\ K^{-1}\ mole^{-1}}$) is the universal gas constant, is here assumed independent of pressure. Eliminating stress and strain-rate from eqs (10), (1) and (2), we obtain an expression for the homologous temperature T/T_m in terms of the absolute rheological coefficients A and a, obtained from measurements of olivine deforming under uniaxial compression (Karato *et al.* 1986), and the apparent rheological coefficient B inferred from the 2-D slab models:

$$\frac{T}{T_m} = \frac{a}{[\ln A + n \ln B + (n+1)\ln\sqrt{3/2}]}. \tag{11}$$

Karato *et al.* (1986) determined flow-law parameters for the deformation of dry olivine: $n = 3.5$, $A = 2.4 \times 10^5\ \mathrm{MPa^{-7/2}\ s^{-1}}$, $H = 540\ \mathrm{kJ\ mol^{-1}}$, and with $T_m = 2140$ K, $a = 30.4$. Then, using $F = 0.2$ and the other slab parameters as estimated above, inversion of (8a) gives $B = 4.6 \times 10^6\ \mathrm{MPa\ s^{2/7}}$. From (11) we then obtain $T/T_m = 0.45$ as an estimate of the apparent homologous temperature of the subducted slab. Bearing in mind that we are comparing the behaviour of a real layered slab that undergoes at least one major phase change with a simplified homogeneous model slab, this estimate is clearly a zeroth-order estimate of some kind of average homologous temperature of the entire subducted slab. This homologous temperature corresponds at lithospheric pressures to a slab temperature of approximately 700°C, and at 600 km to a slab temperature of about 900°C. If the above estimate was based instead on the creep-law parameters for wet olivine (Karato *et al.* 1986), the constraint from the buoyancy ratio would require that the homologous temperature of the slab is only about $T/T_m = 0.40$ (approximately 590°C at lithospheric pressures). On the other hand, if the estimate was based on the creep strength of spinel, which is thought to be greater than that of olivine (Karato 1997), a greater homologous temperature would be inferred.

These estimates of slab homologous temperature are a convenient measure of slab viscosity, a property which is otherwise difficult to characterize in a situation where stress and strain-rate vary greatly. The estimates are in some sense volumetric averages, which are consistent with thermal models of subducted slabs. McKenzie (1969, Fig. 4) estimated the maximum depth of the 640°C isotherm in the Tonga–Kermadec slab, showing that it varies from about 200 km depth beneath New Zealand to about 500 km beneath Tonga. Molnar *et al.* (1979) estimated potential temperatures in slabs at the level of the deepest earthquakes and found potential temperatures remarkably constant with respect to depth, in the range 700 to 900 K. The general agreement between our estimates of slab temperature based on rheological behaviour and those derived from thermal models of subduction, lends support to our interpretation that the buoyancy number of the Tonga–Kermadec slab is at the critical value for buckling to occur.

For either linear or non-linear rheology, our estimates of slab strength validate a key assumption of the model: the slab is much stronger than the convecting mantle into which it descends.

DISCUSSION

The dependence of slab deformation on the buoyancy parameter, F, and the density jump at 670 km, R, in the model is probably a good guide to the influence of buoyancy forces on lithospheric slab deformation in the real Earth. However, the frictional force acting on the lower part of the slab is somewhat artificial and we draw no conclusions from the dependence of the model on parameter k; rather, we concentrate on behaviour that is demonstrably only weakly dependent on k. In reality, frictional forces acting on the slab are part of the interaction with the remaining mantle, but we have assumed that this interaction is of secondary importance in determining the deformation of the subducted slab. This assumption is most likely to be valid if the slab dip is near vertical and if trench migration is not significant. In future calculations we plan to incorporate an asthenospheric pressure difference across the slab to model the effects of general mantle flow and viscous resistance, but we do not anticipate any qualitative changes to the conclusions for buoyancy effects made in this paper. Interpretation of slab–mantle interaction is made doubly difficult because it depends on the entire subduction history (age of lithosphere, pre-existence of faults, etc.), which is unknown.

The assumption of homogeneous density and viscosity in the slab omits several interesting aspects of the real slab deformation problem. First, the effect of a major density anomaly in the slab due to elevation or depression of the olivine–spinel phase boundary at 400 km could have a significant influence on whether down-dip extension or compression dominates within the slab (Goto *et al.* 1987). Second, if the effect of variation in lithospheric viscosity (η or B) across the slab is included, its load-bearing capacity would then be greater on the crustal (colder) side, and the resulting asymmetry would influence the viscous flexural deformation of the slab. Third, and perhaps most importantly, the thermal re-equilibration of the slab also causes its density to change relative to the background mantle, thereby decreasing the buoyancy force and the resistance to deformation with increasing depth in the mantle.

Some subducted slabs appear to level out at 670 km (van der Hilst *et al.* 1991; Fukao *et al.* 1992). This suggests some kind of density jump, although the question of whether the density interface is caused by a phase change or by a compositional difference is not addressed here. In all our experiments, the slab at first penetrates some distance below the 670 km level until the positive buoyancy of the slab segment below 670 km causes it to rotate either clockwise or anticlockwise so that it can return to its depth of minimum gravitational potential at 670 km. The maximum depth to which the slab penetrates varies inversely with the density contrast between the slab and the lower mantle. With $R = -1$, the slab typically descends to between 150 and 250 km below the density discontinuity. When $R = -0.25$, in an experiment with $F = 0.05$ and $n = 1$, the slab descends to 400 km below the density discontinuity before starting to ascend.

In each case, however, the maximum depth we report is associated with the transient effect of the leading end of the slab going through the density discontinuity. After the rollover or buckling has occurred, the maximum depth of the slab below the 670 km level is typically of the order of the slab thickness L. The main effect of reducing the density contrast between the slab and the lower mantle is to increase the time taken for the buckling instability and to increase the maximum depth in the transient stage. This transient behaviour of the slab after it first penetrates the 670 km level offers one explanation of why tomographic images of subduction zones (van der Hilst *et al.* 1991; Fukao *et al.* 1992; van der Hilst 1995) appear in some cases to show the slab flattening out at 670 km, and in other cases to show the slab descending below 670 km. The range of observed slab geometries at the 670 km level can also be explained, however, by a variable trench migration rate coupled with a step-like increase in viscosity at the 670 km level (Kincaid & Olson 1987; Griffiths *et al.* 1995; Christensen 1996).

We expect retrograde trench migration to occur, as observed experimentally by Kincaid & Olson (1987) and Shemenda (1993), unless the subducting plate is in compression at the subduction zone. An extensional membrane stress in the slab where it bends will have a downward resultant normal to the plane of the slab that must be balanced by an overpressure in the asthenosphere. If the asthenosphere can flow from regions of overpressure to regions of underpressure, for example by trench-parallel flow as inferred from seismic anisotropy by Russo & Silver (1994) in South America and Gledhill & Gubbins (1996) in New Zealand, the subduction point will move in the retrograde direction. Although this overpressure is not properly represented in our model, retrograde trench migration caused the slab in some of our experiments to level out at 670 km and continue horizontally at that level (e.g. Fig. 7) instead of buckling. This type of slab geometry (always associated with retrograde trench migration) has also been observed in various experimental and numerical studies (Kincaid & Olson 1987; Griffiths *et al.* 1995; Guillou-Frottier *et al.* 1995; Christensen 1996), although the resulting slab configuration may be unstable to diapiric instability.

The boudinage instability observed with $n = 3$ at large F (Fig. 8c) is analogous to the process referred to as slab detachment in the 2-D convection calculations of Yoshioka *et al.* (1995). Tomographic images of the Hellenic subduction zone (Spakman *et al.* 1988) suggest that a slab-stretching instability of this nature may have occurred in the Aegean upper mantle.

CONCLUSIONS

The plausible estimates of slab rheological parameters obtained in the previous section demonstrate that the model is broadly consistent with the actual deformation of subducted slabs. The model is highly simplified, however, and we must be cautious when interpreting the results in terms of the Earth. Key aspects of the model are (a) the slab is denser and much more viscous than the asthenosphere, (2) its penetration below 670 km is resisted by a step-like density increase at that level, and (3) the lithosphere has uniform physical properties.

Our experiments show that under these conditions the buoyancy number F (eq. 8) is the principal determinant of the style of deformation of the subducted lithospheric slab. The buoyancy number may be interpreted as the ratio of stress generated by buoyancy ($\Delta\rho gL$) to the viscous stress associated with deformation ($\eta U_0/L$). For constant viscosity ($n = 1$), F less than about 0.02 implies that deformation of the subducted slab is dominated by viscous flexure (Figs 5a and b and 6a and b), which typically shows a neutral surface separating regions in which the principal compressive strain-rate directions are respectively parallel and perpendicular to the surface. For F greater than about 0.1, the additional pull from the weight of the subducted slab causes down-dip extension to dominate the deformation (Figs 5c and d). The net extensional strain of the slab at 670 km may be as much as 100 per cent for F greater than about 0.2. In this regime the slab buckles and is folded on top of itself at the 670 km level; it is in down-dip extension across most of the upper mantle, and the characteristic stress pattern of viscous flexure is only observed at the point of subduction and near 670 km, where the slab is tightly folded (Figs 6c and d). The transition between the two regimes occurs gradually around $F = 0.05$.

With stress-dependent viscosity ($n = 3$) the same transition from viscous flexure to down-dip extension occurs but at the larger buoyancy number $F = 0.2$ (Fig. 8). Flexure and down-dip extension are more concentrated in hinge zones of high strain rate, which separate relatively undeforming segments of the slab.

ACKNOWLEDGMENTS

This research was partially supported by Natural Environment Research Council grant GR3/7699. Thanks to Lynn Evans for contributions to the development of the basil/sybil finite-

element program, to Ross Griffiths for a constructive review, and to S.-I. Karato for discussion and constructive comments on the application of creep deformation laws to the mantle.

REFERENCES

Anderson, D.L., 1987. Thermally induced phase changes, lateral heterogeneity of the mantle, continental roots and deep slab anomalies, *J. geophys. Res.*, **92,** 13 968–13 980.

Apperson, K.D. & Frolich, C., 1987. The relationship between Wadati-Benioff zone geometry and P, T and B axes of intermediate and deep focus earthquakes, *J. geophys. Res.*, **92,** 13 821–13 831.

Barazangi, M., Isacks, B.L., Oliver, J., Dubois, J. & Pascal, G., 1973. Descent of lithosphere beneath New Hebrides, Tonga-Fiji and New Zealand: evidence for detached slabs, *Nature,* **242,** 98–101.

Bird, P., 1978. Stress and temperature in subduction shear zones: Tonga and Mariana, *Geophys. J. R. astr. Soc.,* **55,** 411–434.

Caldwell, J.G., Haxby, W.F., Karig, D.E. & Turcotte, D.L., 1976. On the applicability of a universal elastic trench profile, *Earth planet. Sci. Lett.,* **31,** 239–246.

Christensen, U.R., 1996. The influence of trench migration on slab penetration into the lower mantle, *Earth planet. Sci. Lett.,* **140,** 27–39.

Christensen, U.R. & Yuen, D.A., 1984. The interaction of a subducting lithospheric slab with a chemical or phase boundary, *J. geophys. Res.,* **89,** 4389–4402.

Creager, K.C. & Jordan, T.H., 1986. Slab penetration into the lower mantle beneath the Mariana and other island arcs of the northwest Pacific, *J. geophys. Res.,* **91,** 3573–3589.

Cruickshank, J.O. & Munson, B.R., 1981. Viscous fluid buckling of plane and axisymmetric jets, *J. Fluid Mech.,* **113,** 221–239.

Davies, G.F., 1995. Penetration of plates and plumes through the mantle transition zone, *Earth planet. Sci. Lett.,* **133,** 507–516.

Fischer, K.M. & Jordan, T.H., 1991. Seismic strain rate and deep slab deformation in Tonga, *J. geophys. Res.,* **96,** 14 429–14 444.

Fischer, K.M., Creager, K.C. & Jordan, T.H., 1991. Mapping the Tonga Slab, *J. geophys. Res.,* **96,** 14 403–14 427.

Fujita, K. & Kanamori, H., 1981. Double seismic zones and stresses of intermediate depth earthquakes, *Geophys. J. R. astr. Soc.,* **66,** 131–156.

Fukao, Y., Obayashi, M., Inoue, H. & Nenbai, M., 1992. Subducting slabs stagnant in the mantle transition zone, *J. geophys. Res.,* **97,** 4809–4822.

Gaherty, J.B. & Hager, B.H., 1994. Compositional vs. thermal buoyancy and the evolution of subducted lithosphere, *Geophys. Res. Lett.,* **21,** 141–144.

Garfunkel, Z., Anderson, C.A. & Schubert, G., 1986. Mantle circulation and the lateral migration of subducted slabs, *J. geophys Res.,* **91,** 7205–7224.

Giardini, D. & Woodhouse, J.H., 1984. Deep seismicity and modes of deformation in Tonga subduction zone, *Nature,* **307,** 505–509.

Giardini, D. & Woodhouse, J.H., 1986. Horizontal shear flow in the mantle beneath the Tonga arc, *Nature,* **319,** 551–555.

Gledhill, K. & Gubbins, D., 1996. SKS splitting and the seismic anisotropy of the mantle beneath the Hikurangi subduction zone, New Zealand, *Phys. Earth planet. Inter.,* **95,** 227–236.

Goto, K., Suzuki, Z. & Hamaguchi, H., 1987. Stress distribution due to olivine–spinel phase transition in descending plate and deep focus earthquakes, *J. geophys. Res.,* **92,** 13 811–13 820.

Griffiths, R.W. & Turner, J.S., 1988. Folding of viscous plumes impinging on a density or viscosity interface, *Geophys. J.,* **95,** 397–420.

Griffiths, R.W., Hackney, R.I. & van der Hilst, R., 1995. A laboratory investigation of trench migration on the descent of subducted slabs, *Earth planet. Sci. Lett.,* **133,** 1–18.

Guillou-Frottier, L., Buttles, J. & Olson, P., 1995. Laboratory experiments on the structure of subducted lithosphere, *Earth planet. Sci. Lett.,* **133,** 19–34.

Gurnis, M. & Hager, B., 1988. Controls on the structure of subducted slabs, *Nature,* **335,** 317–321.

Hamburger, M.W. & Isacks, B.L., 1987. Deep earthquakes in the southwest Pacific: a tectonic interpretation, *J. geophys. Res.,* **92,** 13 841–13 854.

Hasegawa, A., Umino, N. & Takagi, A., 1978. Double-planed structure of the deep seismic zone in the Northeastern Japan arc, *Tectonophysics,* **47,** 43–58.

Helffrich, G.R., Stein, S. & Wood, B.J., 1989. Subduction zone thermal structure and mineralogy and their relationship to seismic wave reflections and conversions at the slab/mantle interface, *J. geophys. Res.,* **94,** 753–763.

Hirth, G. & Kohlstedt, D.L., 1996. Water in the oceanic upper mantle: implications for rheology, melt extraction and the evolution of the lithosphere, *Earth planet. Sci. Lett.,* **144,** 93–108.

Holt, W.E., 1995. Flow fields within the Tonga slab determined from the moment tensors of deep earthquakes, *Geophys. Res. Lett.,* **22,** 989–992.

Houseman, G. & England, P., 1986. Finite strain calculations of continental deformation 1. Method and general results for convergent zones, *J. geophys. Res.,* **91,** 3651–3663.

Hsui, A.T., Tang, X.-M. & Toksoz, M.N., 1990. On the dip angle of subducting plates, *Tectonophysics,* **179,** 163–175.

Huebner, K.H., 1975. *The Finite Element Method for Engineers,* John Wiley, New York, NY.

Isacks, B. & Molnar, P., 1969. Mantle earthquake mechanisms and the sinking of the lithosphere, *Nature,* **223,** 1121–1124.

Isacks, B.L. & Barazangi, M., 1977. Geometry of Benioff zones: lateral segmentation and downwards bending of the subducted lithosphere, in *Island Arcs, Deep Sea Trenches and Back-Arc Basins,* pp. 99–114, eds. Talwani, M. & Pitman III, W.C., Am. Geophys. Un., Washington, DC.

Ito, E. & Takahashi, E., 1989. Postspinel transformations in the system Mg_2SiO_4-Fe_2SiO_4 and some geophysical implications, *J. geophys. Res.,* **94,** 10 637–10 646.

Jackson, I. & Rigden, S., 1996. Residual uncertainties in the thermoelastic properties of silicate perovskite: implications for the composition and temperature of the Earth's lower mantle, *EOS, Trans. Am. geophys. Un.,* **77** (22), 135.

Jeanloz, R., 1989. High pressure chemistry of the Earth's mantle and core, in *Mantle Convection: Plate Tectonics and Global Dynamics,* pp. 203–260, ed. Peltier, W.R., Gordon and Breach Science Publishers, New York, NY.

Jordan, T.H., Lerner-Lam, A.L. & Creager, K.C., 1989. Seismic imaging of mantle convection: the evidence for deep circulation, in *Mantle Convection: Plate Tectonics and Global Dynamics,* pp. 87–201, ed. Peltier, W.R., Gordon and Breach Science Publishers, New York, NY.

Karato, S.-I., 1997. Phase transformations and rheological properties of mantle minerals, in *Earth's Deep Interior,* eds Crossley, D. & Soward, A.M., Gordon and Breach Science Publishers, in press.

Karato, S.-I., Paterson, M.S. & Fitzgerald, J.D., 1986. Rheology of synthetic olivine aggregates: influence of grain size and water, *J. geophys. Res.,* **91,** 8151–8176.

Kincaid, C. & Olson, P., 1987. An experimental study of subduction and slab migration, *J. geophys. Res.,* **92,** 13 832–13 840.

King, S.D. & Ita, J., 1995. Effect of slab rheology on mass transport across a phase transition boundary, *J. geophys. Res.,* **100,** 20 211–20 222.

Kirby, S.H., 1987. Localized polymorphic phase transformations in high-pressure faults and applications to the physical mechanism of deep earthquakes, *J. geophys. Res.,* **92,** 13 789–13 800.

Lay, T., 1994. Seismological constraints on the velocity structure and fate of subducting lithospheric slabs: 25 years of progress, *Advances in Geophysics,* **35,** 1–180.

Lundgren, P. & Giardini, D., 1994. Isolated deep earthquakes and the fate of subduction in the mantle, *J. geophys. Res.,* **99,** 15 833–15 842.

McKenzie, D.P., 1969. Speculations on the consequences and causes of plate motions, *Geophys. J. R. astr. Soc.*, **18,** 1–32.

Molnar, P., Freedman, D. & Shih, J.S.F., 1979. Lengths of intermediate and deep seismic zones and temperatures in downgoing slabs of lithosphere, *Geophys. J. R. astr. Soc.*, **56,** 41–54.

Nakada, M. & Lambeck, K., 1989. Late Pleistocene and Holocene sea-level change in the Australian region and mantle rheology, *Geophys. J.*, **96,** 497–517.

Ohtaki, T. & Kaneshima, S., 1994. Continuous high velocity aseismic zone beneath the Izu-Bonin arc, *Geophys. Res. Lett.*, **21,** 1–4.

Ringwood, A.E. & Irifune, T., 1988. Nature of the 650 km seismic discontinuity: implications for mantle dynamics and differentiation, *Nature,* **331,** 131–136.

Russo, R.M. & Silver, P.G., 1994. Trench-parallel flow beneath the Nazca plate from seismic anisotropy, *Science,* **263,** 1105–1111.

Shemenda, A.I., 1993. Subduction of the lithosphere and back-arc dynamics: insights from physical modelling, *J. geophys. Res.*, **98,** 16 167–16 185.

Spakman, W., Wortel, M.J.R. & Vlaar, N.J., 1988. The Hellenic subduction zone: a tomographic image and its geodynamic implications, *Geophys. Res. Lett.*, **15,** 60–63.

Tackley, P.J., Stevenson, D.J., Glatzmaier, G.A. & Schubert, G., 1993. Effects of an endothermic phase transition at 670 km depth in a spherical model of convection in the Earth's mantle, *Nature,* **361,** 699–704.

Tao, W.C. & O'Connell, R.J., 1993. Deformation of a weak subducted slab and variation of seismicity with depth, *Nature,* **361,** 626–628.

van der Hilst, R., 1995. Complex morphology of subducted lithosphere in the mantle beneath the Tonga trench, *Nature,* **374,** 154–157.

van der Hilst, R., Engdahl, E.R., Spakman, W. & Nolet, G., 1991. Tomographic imaging of subducted lithosphere below northwest Pacific island arcs, *Nature,* **353,** 37–43.

Vassiliou, M.S., 1984. The state of stress in subducting slabs as revealed by earthquakes analysed by moment tensor inversion, *Earth planet. Sci. Lett.*, **69,** 195–202.

Vinnik, L.P. & Kind, R., 1993. Ellipticity of teleseismic *S*-particle motion, *Geophys. J. Int.*, **113,** 165–174.

Wortel, R., 1982. Seismicity and rheology of subducted slabs, *Nature,* **296,** 553–556.

Wortel, M.J.R. & Spakman, W., 1992. Structure and dynamics of subducted lithosphere in the Mediterranean region, *Proc. Kon. Ned. Akad. v. Wetensch,* **95** (3), 325–347.

Wortel, M.J.R. & Vlaar, N.J., 1988. Subduction zone seismicity and the thermo-mechanical evolution of down-going lithosphere, *Pure appl. Geophys.*, **128,** 625–659.

Yamada, Y., Ito, K., Yokouchi, Y., Tamano, Y. & Ohtsubo, T., 1975. Finite element analysis of steady fluid and metal flow, in *Finite Elements in Fluids,* Vol. 1, pp. 73–94, eds Gallagher, R.H., Oden, J.T., Taylor, C. & Zienkiewicz, O.C., John Wiley, New York, NY.

Yoshioka, S. & Wortel, M.J.R., 1995. Three-dimensional numerical modelling of detachment of subducted lithosphere, *J. geophys. Res.*, **100,** 20 223–20 244.

Yoshioka, S., Yuen, D.A. & Larsen, T.B., 1995. Slab weakening: Mechanical and thermal–mechanical consequences for slab detachment, *The Island Arc,* **4,** 89–103.

Zhong, S. & Gurnis, M., 1995. Mantle convection with plates and mobile faulted plate margins, *Science,* **267,** 838–843.

Zhou, H.-W., 1990. Mapping of P-wave slab anomalies beneath the Tonga, Kermadec and New Hebrides arcs, *Phys. Earth planet. Inter.*, **61,** 199–229.

Zhou, H.-W. & Clayton, R.W., 1990. P and S wave travel time inversions for subducting slab under the island arcs of the northwest Pacific, *J. geophys. Res.*, **95,** 6829–6851.